Simulation and Projection of the Southern Hemisphere Annular Mode in CMIP5 Models

FEI ZHENG

State Key Laboratory of Numerical Modeling for Atmospheric Sciences and Geophysical Fluid Dynamics, Institute of Atmospheric Physics, Chinese Academy of Sciences, and University of Chinese Academy of Science, Beijing, China

JIANPING LI

State Key Laboratory of Numerical Modeling for Atmospheric Sciences and Geophysical Fluid Dynamics, Institute of Atmospheric Physics, Chinese Academy of Sciences, Beijing, China

ROBIN T. CLARK

Met Office Hadley Centre, Exeter, United Kingdom

HYACINTH C. NNAMCHI

State Key Laboratory of Numerical Modeling for Atmospheric Sciences and Geophysical Fluid Dynamics, Institute of Atmospheric Physics, Chinese Academy of Sciences, and University of Chinese Academy of Science, Beijing, China

(Manuscript received 1 April 2013, in final form 3 July 2013)

ABSTRACT

Climate variability in the Southern Hemisphere (SH) extratropical regions is dominated by the SH annular mode (SAM). Future changes in the SAM could have a large influence on the climate over broad regions. In this paper, the authors utilized model simulations from phase 5 of the Coupled Model Intercomparison Project (CMIP5) to examine projected future changes in the SAM during the austral summer [December–February (DJF)]. To start off, first, the ability of the models in reproducing the recently observed spatial and temporal variability was assessed. The 12 CMIP5 models examined were found to reproduce the SAM's spatial pattern reasonably well in terms of both the symmetrical and the asymmetric component. The CMIP5 models show an improvement over phase 3 of CMIP (CMIP3) in simulating the seesaw structure of the SAM and also give improvements in the recently observed positive SAM trend. However, only half the models appeared to be able to capture two major recent decadal SAM phases. Then, the future SAM trends and its sensitivity to greenhouse gas (GHG) concentrations using simulations based on the representative concentration pathways 4.5 (RCP4.5) and 8.5 (RCP8.5) were explored. With RCP4.5, a very weak negative trend for this century is found. Conversely, with RCP8.5, a significant positive trend was projected, with a magnitude similar to the recently observed trend. Finally, model uncertainty in the future SAM projections was quantified by comparing projections from the individual CMIP5 models. The results imply the response of SH polar region stratospheric temperature to GHGs could be a significant controlling factor on the future evolution of the SAM.

1. Introduction

The Southern Hemisphere (SH) annular mode (SAM), also known as the Antarctic Oscillation (AAO), dominates climate variability in extratropical regions over the Southern Hemisphere (Gong and Wang 1998, 1999; Thompson and Wallace 2000; Thompson et al. 2000). The SAM is characterized by a shift of the jet position between mid- and high latitudes. During positive phases, the belt of westerly winds shifts toward Antarctica. When negative, displacement is equatorward. The SAM owes its existence mainly to internal atmospheric dynamics related to wave–current interactions (Limpasuvan and Hartmann 1999; Lorenz and Hartmann 2001). Li and Wang (2003) proposed the concept of the atmospheric annular belts of actions (ABAs), which are hemispheric-wide

---

Corresponding author address: Dr. Jianping Li, Deputy Director and Professor, State Key Laboratory of Numerical Modeling for Atmospheric Sciences and Geophysical Fluid Dynamics, Institute of Atmospheric Physics, Chinese Academy of Sciences, P.O. Box 9804, Beijing 100029, China.
E-mail: ljp@lasg.iap.ac.cn

DOI: 10.1175/JCLI-D-13-00204.1

TABLE 1. List of CMIP5 models included in this study and complete expansions for models and model centers.

Name	Model center	Ensemble size		Output data			
		Historical	RCP4.5 (RCP8.5)	Resolution (°lat × °lon)	Vertical levels	Model top height (hPa)	Reference
Second Generation Canadian Earth System Model (CanESM2)	Canadian Centre for Climate Modelling and Analysis (CCCma), Canada	5	5 (5)	64 × 128	22	1	Chylek et al. (2011)
Community Climate System Model, version 4 (CCSM4)	National Center for Atmospheric Research (NCAR), United States	6	5 (5)	192 × 288	17	2.194067	Gent et al. (2011)
Centre National de Recherches Météorologiques Coupled Global Climate Model, version 5 (CNRM-CM5)	Centre National de Recherches Météorologiques (CNRM), France	10	1 (1)	128 × 256	17	10	Voldoire et al. (2013)
Flexible Global Ocean–Atmosphere–Land System Model gridpoint, version 2.0 (FGOALS-g2)	The State Key Laboratory of Numerical Modeling for Atmospheric Sciences and Geophysical Fluid Dynamics (LASG), China	5	1 (1)	60 × 128	17	2.19	Yu et al. (2011)
Goddard Institute for Space Studies Model E2, coupled with the Hybrid Coordinate Ocean Model (HYCOM) ocean model (GISS-E2-H)	National Aeronautics and Space Administration (NASA), United States	5	3 (0)	89 × 144	17	0.1	—
Hadley Centre Coupled Model, version 3 (HadCM3)	Met Office Hadley Centre (MOHC), United Kingdom	10	3 (0)	73 × 96	17	10	Gordon et al. (2000)
Model for Interdisciplinary Research on Climate, Earth System Model, Chemistry coupled (MIROC-ESM-CHEM)	Japan Agency for Marine-Earth Science and Technology (JAMSTEC), Atmosphere and Ocean Research Institute (The University of Tokyo), and National Institute for Environmental Studies, Japan	1	1 (1)	64 × 128	35	0.0036	Watanabe et al. (2011)
Model for Interdisciplinary Research on Climate, Earth System Model (MIROC-ESM)	JAMSTEC, Atmosphere and Ocean Research Institute (The University of Tokyo), and National Institute for Environmental Studies, Japan	3	1 (1)	64 × 128	35	0.0036	Watanabe et al. (2011)
Max Planck Institute Earth System Model, low resolution (MPI-ESM-LR)	Max Planck Institute for Meteorology (MPI), Germany	3	3 (3)	96 × 192	25	0.01	—
Meteorological Research Institute Coupled Atmosphere–Ocean General Circulation Model, version 3 (MRI-CGCM3)	Meteorological Research Institute (MRI), Japan	3	1 (1)	160 × 320	23	0.01	Yukimoto et al. (2012)
Flexible Global Ocean–Atmosphere–Land System Model, second spectral version (FGOALS-s2)	LASG, China	3	3 (3)	108 × 128	17	2.19	Bao et al. (2013)
Beijing Climate Center, Climate System Model, version 1.1 (BCC_CSM1.1)	Beijing Climate Center (BCC), China Meteorological Administration, China	1	1 (1)	64 × 128	17	2.917	Jiang et al. (2010)

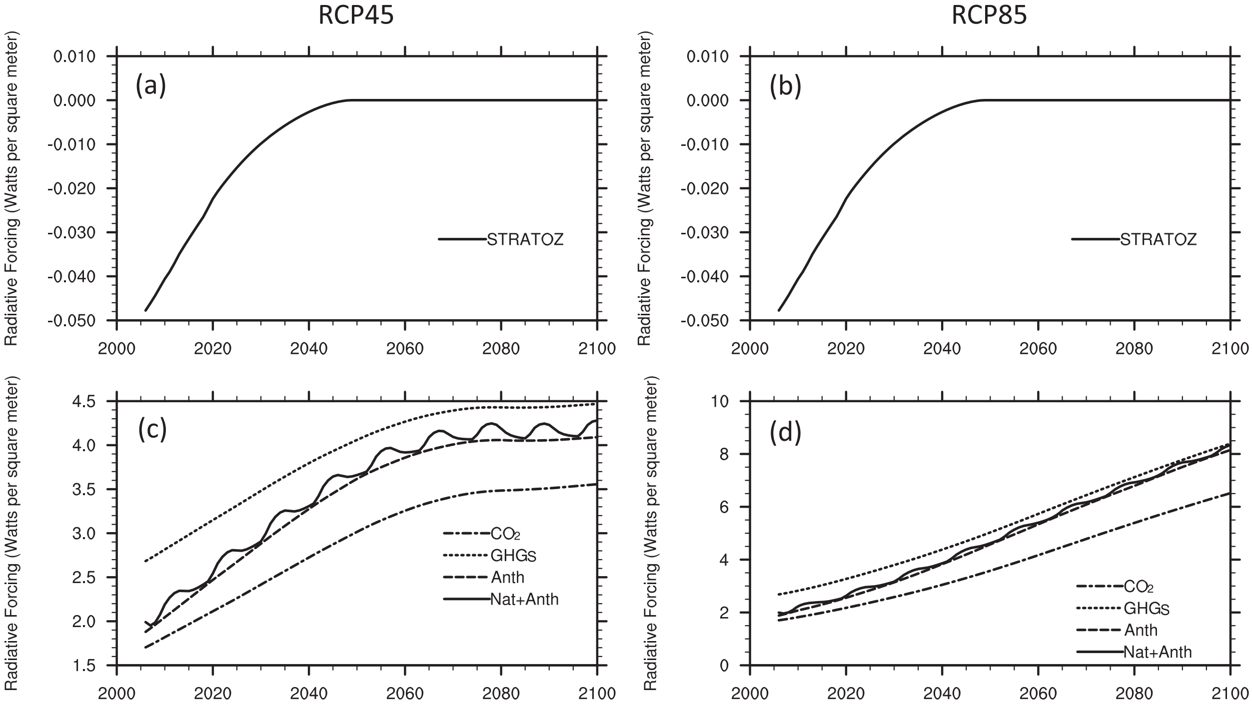

FIG. 1. Temporal evolution of radiative forcing (W m^{-2}) caused by (a),(b) stratospheric ozone (STRATOZ) and (c),(d) CO_2, GHGs, anthropogenic factors (Anth) and natural and anthropogenic factors as a whole (Nat + Anth) under (left) RCP4.5 and (right) RCP8.5. GHGs represent total GHGs forcing, including CO_2, CH_4, N_2O, HFCs, PFCs, SF_6, and other Montreal Protocol gases. Note that STRATOZ is the same under RCP4.5 and RCP8.5.

fluctuations in air mass between mid- and high latitudes associated with the Ferrel cell, extending the understanding of the physical mechanism of the annular mode.

The SAM has a significant influence on the climate of Antarctica (Schneider et al. 2004; Marshall et al. 2006; Ciasto and Thompson 2008; Simpkins et al. 2012) and also more generally over a large part of the SH (Thompson et al. 2011). For instance, both observation and model representation illustrated the SH ocean temperature, in particular, and coupled ocean–atmosphere–ice system, in general, responses to the SAM variations (Kwok and Comiso 2002; Lefebvre et al. 2004; Renwick and Thompson 2006; Sen Gupta and England 2006; Hendon et al. 2007; Screen et al. 2010; Ciasto et al. 2011). Recent research found that Hadley cell expansion and subtropical precipitation are also sensitive to SAM changes related to ozone depletion (Previdi and Liepert 2007; Kang et al. 2011). Evidence even suggests an influence of the SAM on climate as far away as the Northern Hemisphere (NH; Nan and Li 2003, 2005a,b; Wu et al. 2006a,b; Gong et al. 2009; Nan et al. 2009; Song et al. 2009; Wu et al. 2009; Li et al. 2011a,b; Zheng and Li 2012; Li et al. 2013). For example, the boreal spring and winter SAM can influence the following season's precipitation over the middle to lower reaches of the Yangtze River and south China through an ''atmospheric–oceanic coupled bridge'' (Nan and Li 2003; Zheng and Li 2012; Li et al. 2013). Wu et al. (2009) revealed that the anomalous positive autumn SAM is associated with a weak winter monsoon in East Asia during the northern winter.

Over recent decades, a positive trend in the SAM has been observed, largely attributed to ozone depletion in the stratosphere above Antarctica (Thompson and Solomon 2002; Gillett and Thompson 2003; Arblaster and Meehl 2006; Polvani et al. 2011a; Thompson et al. 2011). A smaller influence has also been identified related to increasing greenhouse gases (GHGs; Marshall et al. 2004; Shindell and Schmidt 2004; Arblaster and Meehl 2006) and variability in tropical sea surface temperature (SST; Grassi et al. 2005).

Through the twenty-first century, however, stratospheric ozone is expected to recover, raising an interesting question regarding the future development of the SAM. While ozone recovery is likely to give a negative SAM influence (Polvani et al. 2011b), GHGs concentrations are likely to give a positive influence, which could counteract the effect of ozone recovery (McLandress et al. 2011). Accurately handling the two opposing influences from ozone and GHGs will therefore be crucial not only to the projection of future SAM trends but also to statistically downscaling climate

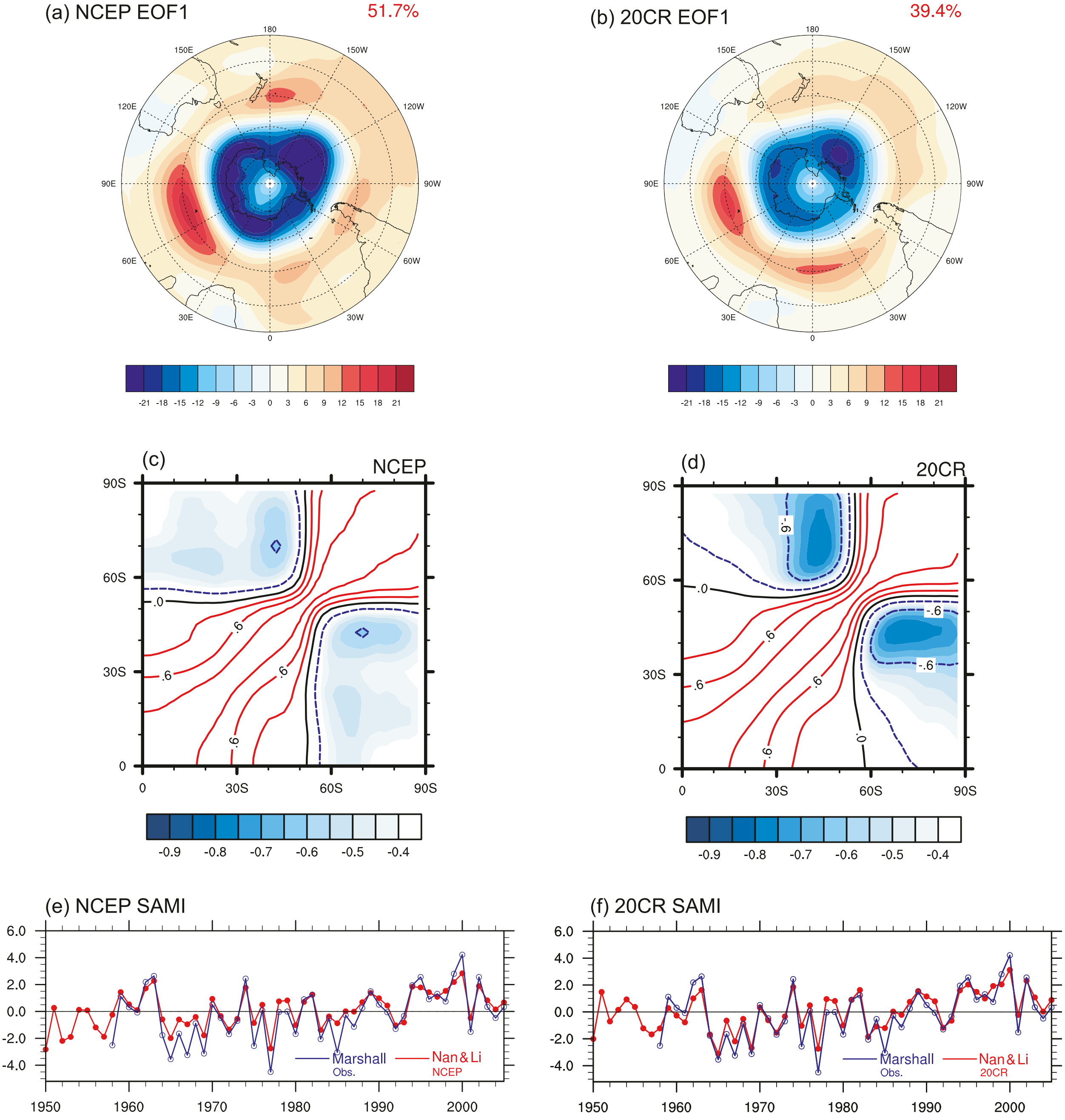

FIG. 2. (a),(b) Spatial pattern of the SAM as the leading EOF mode at 700-hPa geopotential height south of 20°S, (c),(d) cross-correlation coefficients between zonal-averaged SLP anomalies in the SH, and (e),(f) time series of the SAMI determined from (left) NCEP–NCAR reanalysis and (right) 20CR. The station-based SAMI reconstructed by Marshall (2003) is also shown in (e) and (f). The red numbers in (a) and (b) indicate explained variance. In (c) and (d), the contour and shading intervals are 0.3 and 0.05, respectively. The solid (dotted) contours represent positive (negative) values. Note that (c) and (d) are symmetric about the diagonal.

projections in regions where the climate is closely associated with the SAM (i.e., the Antarctic, SH extratropical regions, and even in the NH).

Phase 5 of the Coupled Model Intercomparison Project (CMIP5) provides an opportunity to evaluate the opposing ozone and GHGs effects on the future SAM. We investigate the performance of these state-of-the-art models in reproducing the present-day SAM and, using these results as a baseline, generate projections of the SAM for future scenarios. In fact, simulations and projections of the SAM have been investigated in several studies using phase 3 of CMIP (CMIP3); for example,

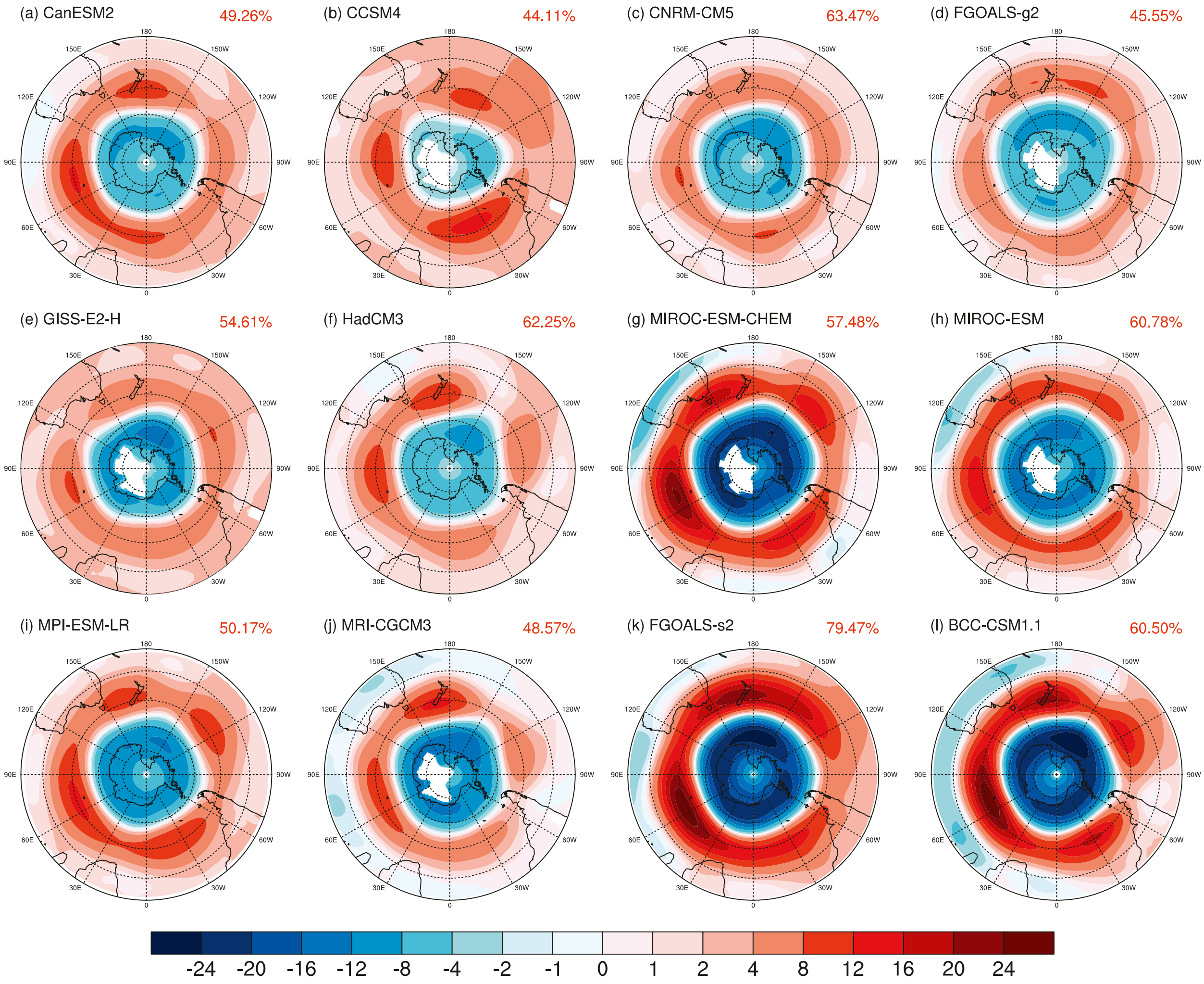

FIG. 3. As in Fig. 2a, but for CMIP5 models.

Cai and Cowan (2007) and Fogt et al. (2009a) found that most CMIP3 models captured the recent positive SAM trends in the austral summer, but models containing time-variable ozone produced larger significant trends. Simpkins and Karpechko (2012) estimated future SAM trends under different Intergovernmental Panel on Climate Change (IPCC) Fourth Assessment Report (AR4) scenarios [Special Report on Emission Scenarios (SRES) B1, A1B, and A2] and explored the sensitivity of the SAM on these GHGs scenarios.

However, most studies evaluating model performance in describing the present-day SAM have focused mainly on the linear trend component. Little research has been devoted to investigating the spatial pattern of the SAM and the reliability of decadal, or even interannual, variability of the modeled SAM. Consequently, we intend to address three main issues in this study. First, we consider how well the CMIP5 models reproduce the SAM pattern and whether the models describe decadal and interannual variability of the SAM as well as the linear trend. In addition, we investigate the likely evolution of the SAM under different scenarios using the multimodel ensemble (MME) in CMIP5, which, in general, contains higher-resolution models than CMIP3. Finally, we consider how models respond differently to similar external forcing and the possible causes of model uncertainty in the SAM projections.

The remainder of this manuscript is organized as follows. In section 2, we briefly introduce the CMIP5 models, reanalysis data, and methods employed in this work, while in section 3 we assess the ability of these models in reproducing the observed spatial patterns and temporal evolution of the SAM. In section 4, we describe changes in the SAM projected over the next 100 years using two GHGs pathways. Analysis of model uncertainty between the SAM projections is discussed in

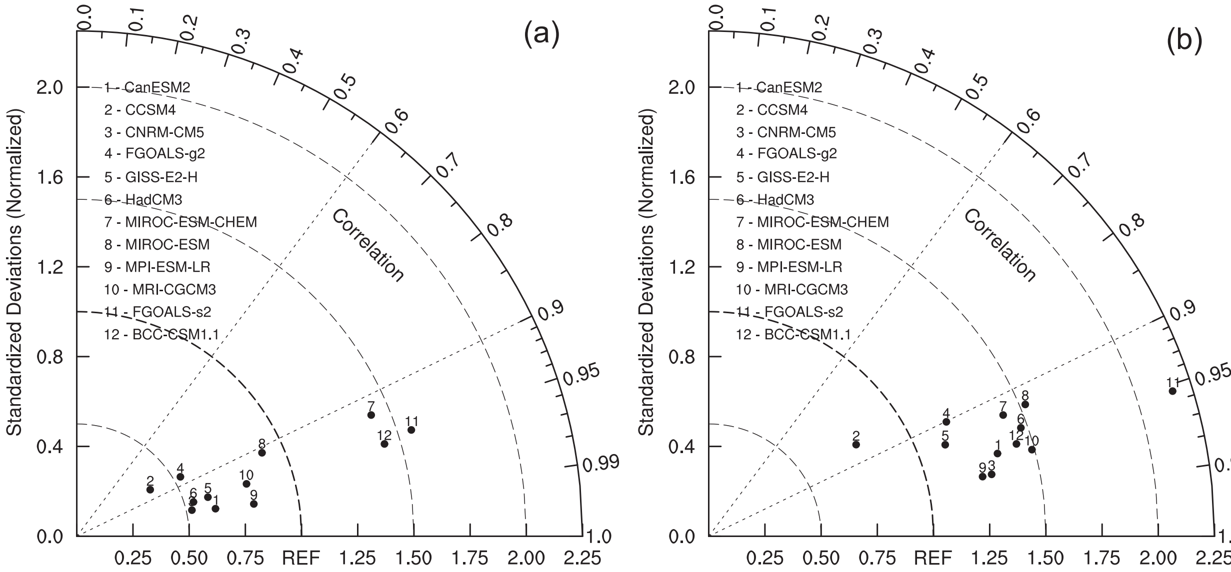

FIG. 4. Taylor diagram of the SAM pattern. (a) Multisimulation ensemble and (b) first simulation member. The solid circles (numbered) refer to the 12 models. The correlation coefficients and the ratio of the standard deviation between modeled and observed (20CR) SAM patterns are shown by the cosine of the azimuth angle and the radial distance, respectively. The term "REF" on the horizontal axis indicates the reference point. All model results have been interpolated to the same horizontal resolution as the observations.

section 5. Finally, discussion and conclusions are presented in section 6.

2. Models, data, and methodology

a. Models

To inform the IPCC's Fifth Assessment Report (AR5) on climate change, the World Climate Research Programme (WCRP) coordinated the CMIP5 project, collating a large set of climate model simulations. The project follows on from the previous CMIP3. However, whereas in CMIP3 ozone concentrations were usually fixed, in the CMIP5 models ozone is time dependent, an essential factor in accurately handling the temporal evolution of ozone destruction and recovery according to findings by Cai and Cowan (2007) and Fogt et al. (2009a).

From the archive, we used data from 12 coupled models developed at 10 modeling centers (see Table 1 for complete list of models with full expansions). Models were selected primarily on the basis of data availability and model diversity. For example, output data from CCSM4, CNRM-CM5, MRI-CGCM3, and FGOALS-s2 have a higher horizontal resolution and MIROC-ESM-CHEM, MIROC-ESM, MPI-ESM-LR, MRI-CGCM3, and CanESM2 have a higher vertical resolution. There are Earth system models, such as CanESM2 and MPI-ESM-LR, which include biological processes governing the variation of the corresponding elements in the Earth system, and atmospheric chemistry coupled models, such as MIROC-ESM-CHEM.

For assessing the ability of the 12 models in simulating the recently observed SAM, we used historical simulations for the 1850–2005 period (Taylor et al. 2012). For future projections, we used simulations based on representative concentration pathways (RCPs; Meinshausen et al. 2011). Among the various RCPs, we focus here on the RCP4.5 and RCP8.5 pathways. These are defined such that their radiative forcing will reach about 4.5 and 8.5 W m^{-2} by the year 2100, respectively. Figure 1 shows the time evolution of radiative forcing under these two pathways. With the RCP4.5 path, GHGs radiative forcing are stabilized before 2100 without overshoot. With RCP8.5, no stabilization occurs before 2100 (Taylor et al. 2012). The forcing from the RCP8.5 pathway is almost twice that of the RCP4.5 pathway by 2100. For both pathways, a single ozone forcing pathway was used with a gradually weakening negative forcing to account for the expected stratospheric ozone recovery during the first half of the twenty-first century. Beyond 2060, the forcing from ozone was held constant at zero.

Multiple, and equally plausible, simulations were available from most models, with differing realizations based solely on the initial conditions. Data from the GISS-E2-H and HadCM3 RCP8.5 simulations were unavailable at the time of writing, so these two models were omitted from our RCP analysis.

b. Reanalysis datasets

For model validation, we used reanalysis data from the National Centers for Environmental Prediction–National

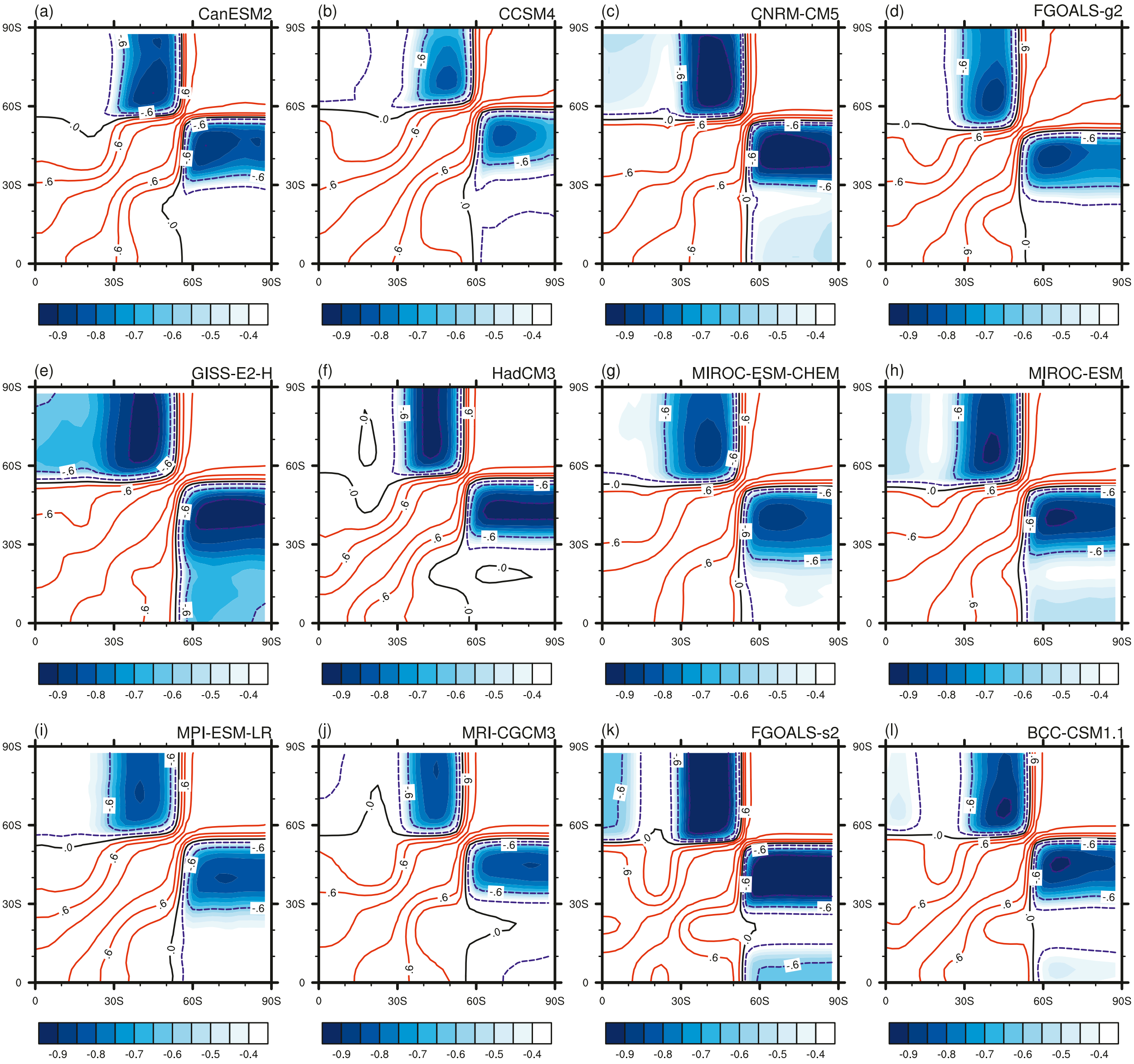

FIG. 5. As in Fig. 2c, but for CMIP5 models. The interpolation method is as in Fig. 4.

Center for Atmospheric Research (NCEP–NCAR) reanalysis 1 (Kalnay et al. 1996) and Twentieth-Century Reanalysis Project, version 2 (20CR; Compo et al. 2011), projects. The horizontal resolution used in the two reanalysis is 2.5° × 2.5° and 2.0° × 2.0° with 17 and 24 vertical levels, respectively.

c. *Methodology*

Since the SAM manifests its greatest variability during the austral summer, we focused on the SH warm season between December and February (inclusive). For the validation, we examine the period 1950–2005, using seasonal means.

In our analysis, we take the SAM pattern to be the leading empirical orthogonal function (EOF) mode of the 700-hPa geopotential height southward of 20°S. Before calculating the mode, the geopotential height is multiplied by cosine (latitude) to ensure equal areas are given equal weight. Assuming $\mathbf{X}$ is the original data matrix with dimension $m \times n$, the EOF analysis can be expressed as follows:

$$\mathbf{X} = \mathbf{EP}, \tag{1}$$

where $\mathbf{E}$ is the $m \times m$ matrix that has EOF loading patterns in its columns, and $\mathbf{P}$ is the $m \times n$ matrix with

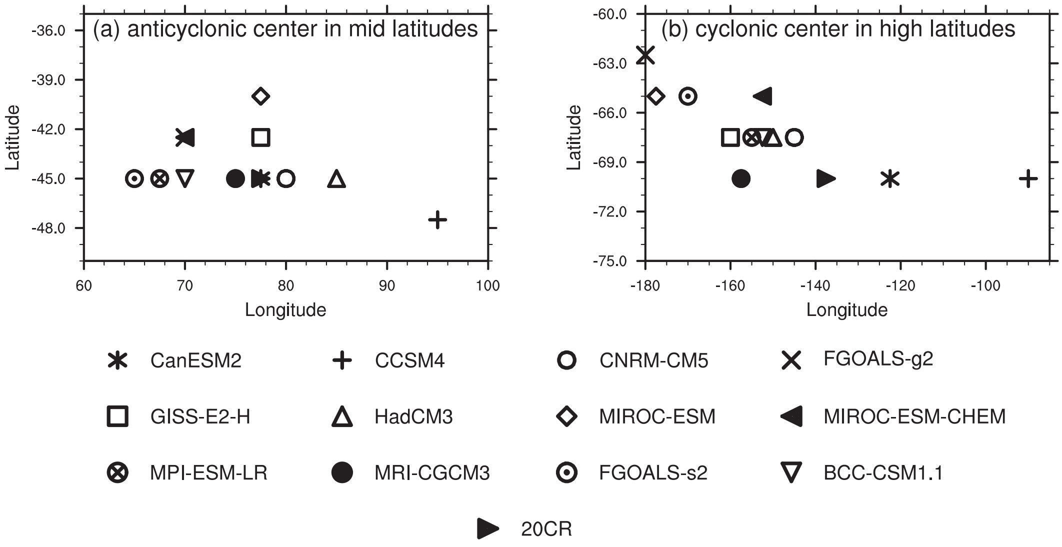

FIG. 6. Locations of (a) the strongest anticyclone center over the southern Indian Ocean and (b) the cyclonic center over the northwestern Antarctic in the SAM pattern. The interpolation method is as in Fig. 4.

principal components (PCs) in its rows. The fitting of $\mathbf{X}$ by the ith EOF mode, referred to as $\hat{\mathbf{X}}_i$, with dimensions $m \times n$, can be written as

$$\hat{\mathbf{X}}_i = \mathbf{E}_i\mathbf{P}_i, \tag{2}$$

where $\mathbf{E}_i$ is a $m \times 1$ vector representing the ith loading pattern, and $\mathbf{P}_i$ is a $1 \times n$ vector representing the ith PC (Storch and Zwiers 1999; Wilks 2006). To enable comparison among $\mathbf{E}_i$ from different models, we normalize $\mathbf{E}_i$ by the standard deviation of the corresponding $\mathbf{P}_i$ to ensure these $\mathbf{E}_i$ are comparable. The normalized loading pattern and PC, referred to as the $\mathbf{NEOF}_i$ and $\mathbf{NPC}_i$, respectively, are defined as

$$\mathbf{NEOF}_i = \sigma_i\mathbf{E}_i, \quad \text{and} \tag{3}$$

$$\mathbf{NPC}_i = \frac{1}{\sigma_i}\mathbf{P}_i, \tag{4}$$

where σ_i is the standard deviation of $\mathbf{P}_i$.

For a numerical SAM quantification, we employed the definition of the SAM index (SAMI) by Nan and Li (2003), which is the difference in the normalized monthly zonal mean sea level pressure (SLP; $\hat{P}$) between 40° and 70°S:

$$\text{SAMI} = \hat{P}_{40°\text{S}} - \hat{P}_{70°\text{S}}. \tag{5}$$

This SAMI definition is widely used in research on the SAM and its climate impact (Nan and Li 2005a,b; Wu et al. 2006a,b; Li and Li 2009, 2010, 2011, 2012; Feng et al. 2010; Zheng and Li 2012; Feng et al. 2013) and is a modification of the AAO index defined by Gong and Wang (1999). In addition, to examine the reliability of reanalysis-based SAMI before the satellite era, the station-based index reconstructed by Marshall (2003) was also analyzed. An equal weighting MME (Deser et al. 2012) approach is used to make future projections of the SAM. We also calculate a selected multimodel ensemble (SMME) mean using models that best reproduce the recently observed trend. The nonparametric Mann–Kendall test is used to assess the significance of the linear trends.

3. Performance of CMIP5 models in reproducing the present-day SAM

a. *Spatial and temporal characteristic of the SAM in observation*

Figure 2 shows the observed SAM patterns and indices for the 1950 to 2005 period determined from the NCEP–NCAR and 20CR reanalyses. The SAM pattern is shown as the leading EOF mode of the 700-hPa geopotential heights southward of 20°S. The positive SAM phase is characterized by lower (higher) geopotential heights over high (mid) latitudes, reflecting an equatorward shift in atmospheric mass. The leading mode accounts for more than 50% of the geopotential height variability during austral warm seasons in the NCEP–NCAR reanalysis but only about 39% in the 20CR. Notwithstanding these differences in the percentage of explained variance, there is good agreement in the spatial patterns of the SAM, with a spatial correlation coefficient of up to 0.98. In addition, considering the

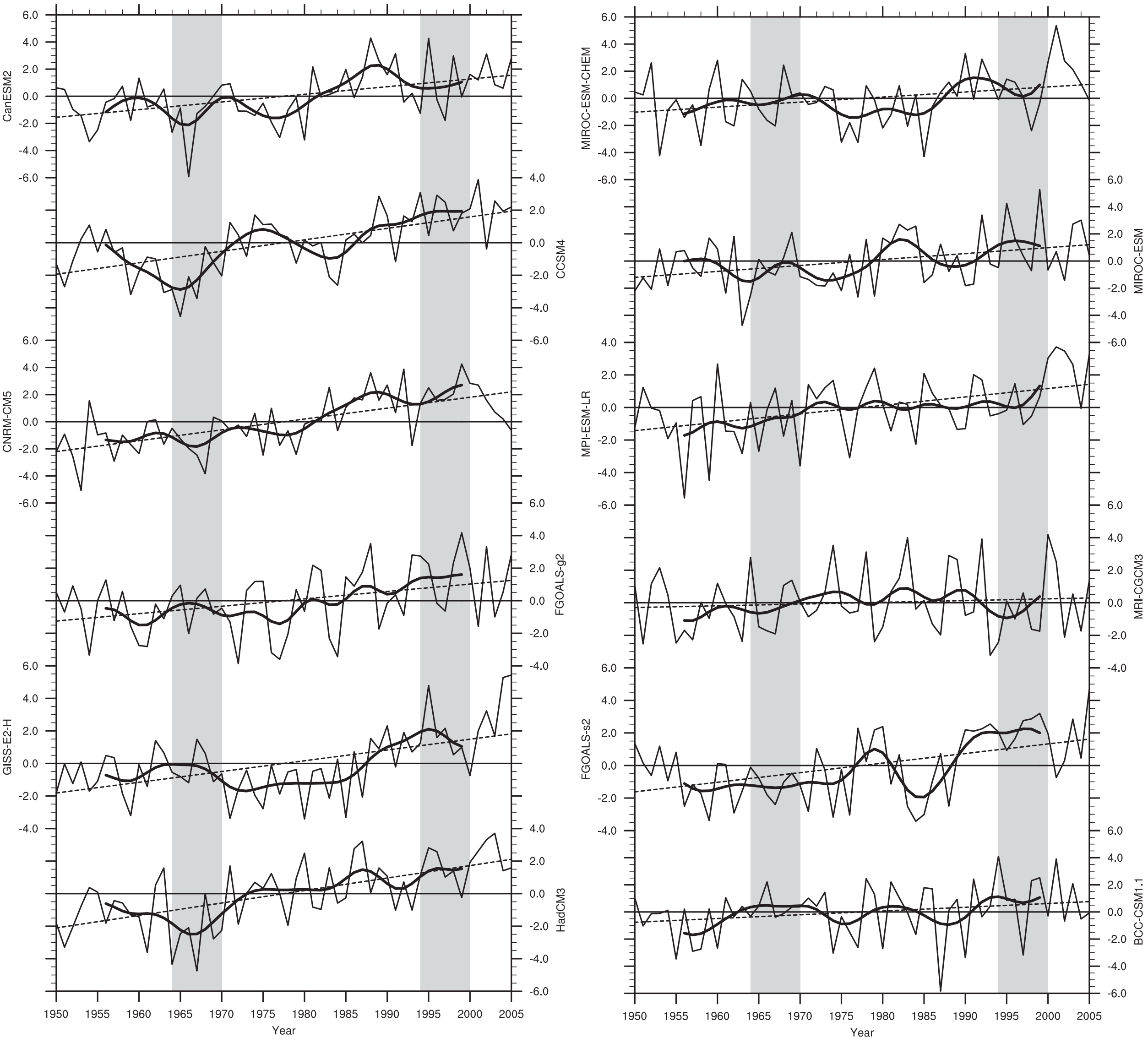

FIG. 7. Time series of the SAMI from CMIP5 models. The thin and thick solid lines denote the raw time series and decadal variability obtained from the 13-yr weighted running average, respectively. The thin dashed lines indicate the linear trend component. The shaded areas cover the two selected periods, 1964–70 and 1994–2000.

possible errors in the SH extratropical reanalysis data before satellite era (Bromwich and Fogt 2004), a similar EOF analysis based on the satellite era–only period of 1980–2005 was conducted (not shown). The results indicate that the SAM patterns obtained by these two periods are quite consistent, especially in the 20CR with a spatial correlation coefficient of 0.96.

Agreements are also observed in the zonal symmetry characteristics of the SAM between the two reanalysis datasets. Figures 2c and 2d show the cross-correlation coefficients between zonally averaged SLP from the reanalysis datasets. With 55° and 60°S as a transition region, pressure patterns in the mid- (30°–55°S) and high latitudes (60°–90°S) are negatively correlated, which is a manifestation of hemispheric-wide fluctuations in air mass between the two ABAs (Li and Wang 2003), reflecting the zonally symmetrical nature of the SAM.

As well as the zonally symmetrical components, asymmetric or nonannular components also exist within the spatial patterns of the SAM (Fan 2007; Meneghini et al. 2007; Marshall et al. 2011; Sun and Li 2012; Liu and Wang 2013). These asymmetric components, in terms of the position and strength of the strongest negative and positive anomaly centers in the two ABAs, are also consistent between the two reanalysis datasets (Figs. 2a,b). For

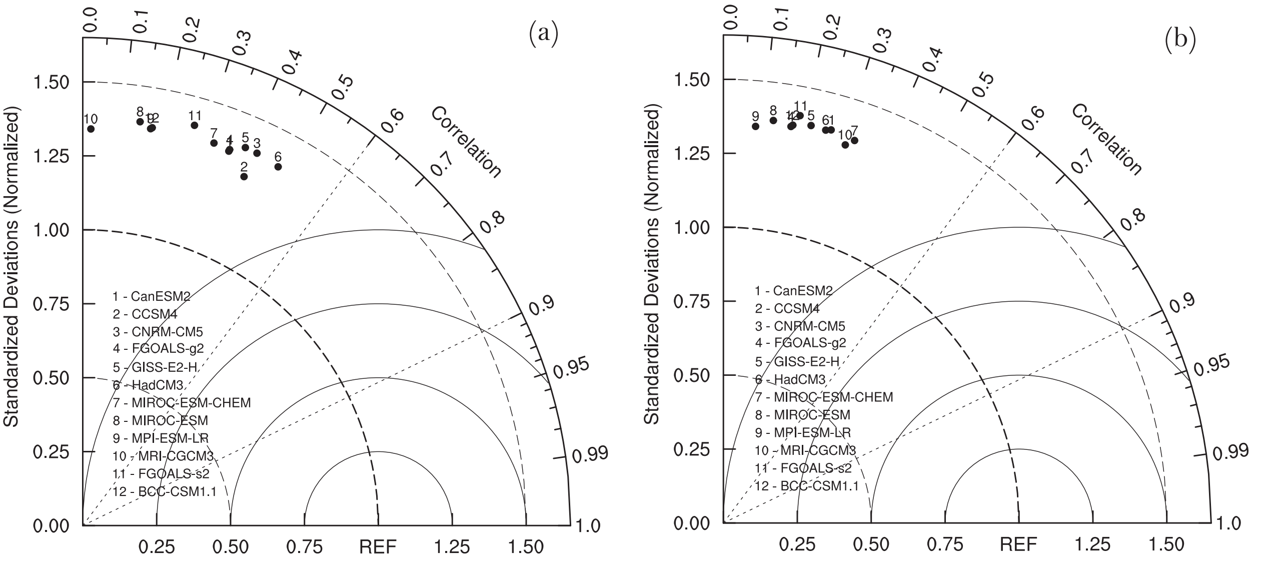

FIG. 8. As in Fig. 4, but for the SAMI.

example, both show a cyclonic center over northwestern Antarctica (60°–75°S, 150°–120°W) and an anticyclonic center over the southern Indian Ocean (40°–50°S, 60°–90°E).

Figures 2e and 2f show the temporal evolution of the SAMI since 1950. The recently observed positive SAMI trend can clearly be seen. It is statistically significant at the 95% confidence level in both reanalysis datasets. In addition, there is obvious decadal variability in the SAMI (Gong and Wang 2001; Visbeck 2009; Yuan and Yonekura 2011). For example, decadal negative and positive phases occurred during the 1960s and 1990s, respectively. The station-based SAMI constructed by Marshall (2003) is also shown in Figs. 2e and 2f. The correlation coefficients between this station-based index and that from the reanalysis are greater than 0.90, implying the consistency of the temporal variations of the SAM among these indices. Besides, the linear trends (1958–2005) derived from the 20CR and Marshall's indices are very close (0.0518 and 0.0465 yr $^{-1}$, respectively).

b. *SAM patterns simulated by individual models*

Figure 3 shows the equivalent results to Fig. 2a but for our 12 CMIP5 models. The explained variances of the SAM as the dominating mode in SH extratropical regions vary considerably among models. Most of the models exaggerate the explained variance, particularly compared to that of the 20CR reanalysis. For example, variances of 63% and 79% are obtained for CNRM-CM5 and FGOALS-s2, respectively, compared to 39% by 20CR.

To quantify the correspondence between modeled and observed (20CR) SAM patterns, a pair of Taylor diagrams (Taylor 2001) are shown in Fig. 4. As Fig. 4a shows, the spatial correlation coefficients between the modeled and observed SAM are greater than 0.85 in all models except for CCSM4 (0.83). This strong correlation indicates that models perform relatively well in simulating the meridional dipole structure of the SAM. Compared with similar Taylor diagram analysis using output from the CMIP3 models by Zhu and Wang (2008), the spatial correlation coefficients in Fig. 4a are mainly higher, implying that the CMIP5 models generally provide a better simulation of the SAM structure than the CMIP3 models.

However, the models performed less well in reproducing the amplitude of the observed SAM pattern. In the Taylor diagram (Fig. 4a), the ratio of the standard deviation of the modeled and observed SAM patterns ranges from about 0.25 to 1.6. Three models (MIROC-ESM-CHEM, FGOALS-s2, and BCC_CSM1.1) exaggerated the amplitude of the SAM pattern, while the other models gave underestimates. For six models in particular (CanESM2, CCSM4, CNRM-CM5, FGOALS-g2, GISS-E2-H, and HadCM3), the ratio was less than 0.75. Interestingly, these six models also contain a relatively large number of ensemble simulation members (Table 1). To explore how ensemble size can influence the simulated spatial amplitude of the SAM, Fig. 4b shows the same as Fig. 4a but only using the first simulation of each model. The ratios in this simulation for all six models appear to increase to larger than 0.75. Compared to individual simulations, the ensemble mean appears to give a reduced SAM signal, possibly arising from damped internal variability in the mean (Deser et al. 2012). For several models, such as CCSM4, this reduction in spatial variability leads

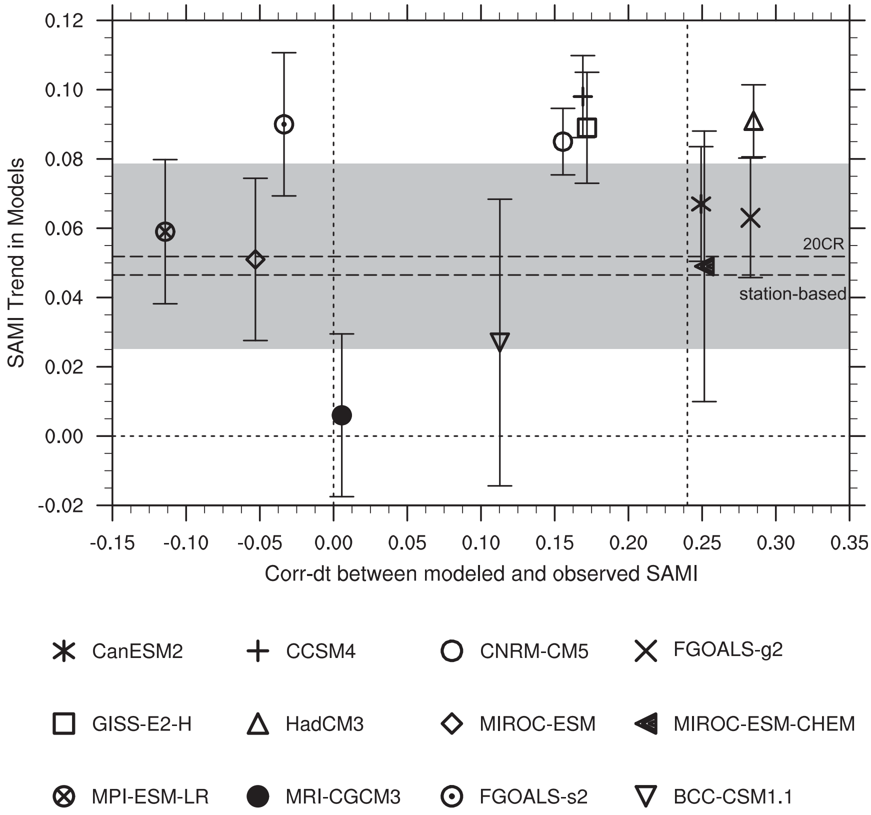

FIG. 9. Scatterplot of the correlation coefficients between modeled and 20CR-derived detrended SAMI against the linear trend in the modeled SAMI. The two long dashed lines indicate the value of the SAMI trend from 20CR and the station-based index reconstructed by Marshall (2003), respectively. The shaded area covers the 95% confidence interval of 20CR. Error bars show the 95% confidence interval for each model, scaled by the square root of the number of ensemble members for each model. The short dashed lines are scale marks. The analyzed period is from 1958 to 2005 because the austral summer seasonal-mean Marshall's index starts from 1958.

to deviation from the observations. However, for a model such as FGOALS-s2 with an overly large ratio, this decrease brings a result closer to the observations (Fig. 4b). Put simply, combining ensemble simulations ameliorate some simulations but worsen others. It is therefore necessary to consider how best to deal with ensemble simulations for any one particular model.

Figure 5 shows the cross correlation of zonally averaged SLP anomalies in the SH in the CMIP5 models, from which we can explore the ability of the models to reproduce zonally symmetrical features of the SAM. The outstanding feature is that the negative correlation between mid- and high latitudes is stronger than in observed situations (Figs. 2c,d). This illustrates that the models magnify the circulation variability associated with the SAM, which is in agreement with the greater explained variance of the modeled SAM patterns (Fig. 3), implying that the models might exaggerate meridional air mass exchanges between mid- and high latitudes. In spite of this overestimate of the strength of the ABAs (Li and Wang 2003), the positions of the ABAs in these models are highly consistent with observations. The transition region between 55° and 60°S is distinct.

Finally for this section, we consider model performance in handling nonannular components of the SAM. Here, we focus on the locations of the cyclonic center over northwestern Antarctica and the anticyclonic center over the southern Indian Ocean, which are both clearly evident in the NCEP–NCAR and 20CR reanalyses as noted above. The locations of the cyclonic and anticyclonic centers were measured as the lowest value within 60°–75°S, 180°–90°W and highest value within 35°–50°S, 60°–100°E, respectively, in the SAM pattern (Fig. 6). The models capture the latitude of the anticyclonic center in midlatitudes reasonably well, with a range of about 7.5° among the models. All models were within 5.5° of the 20CR. By comparison, the spread of longitudes predicted for the anticyclonic center is larger, at about 30°. Similarly, for the cyclonic center at high latitudes, the models reproduced the latitude more

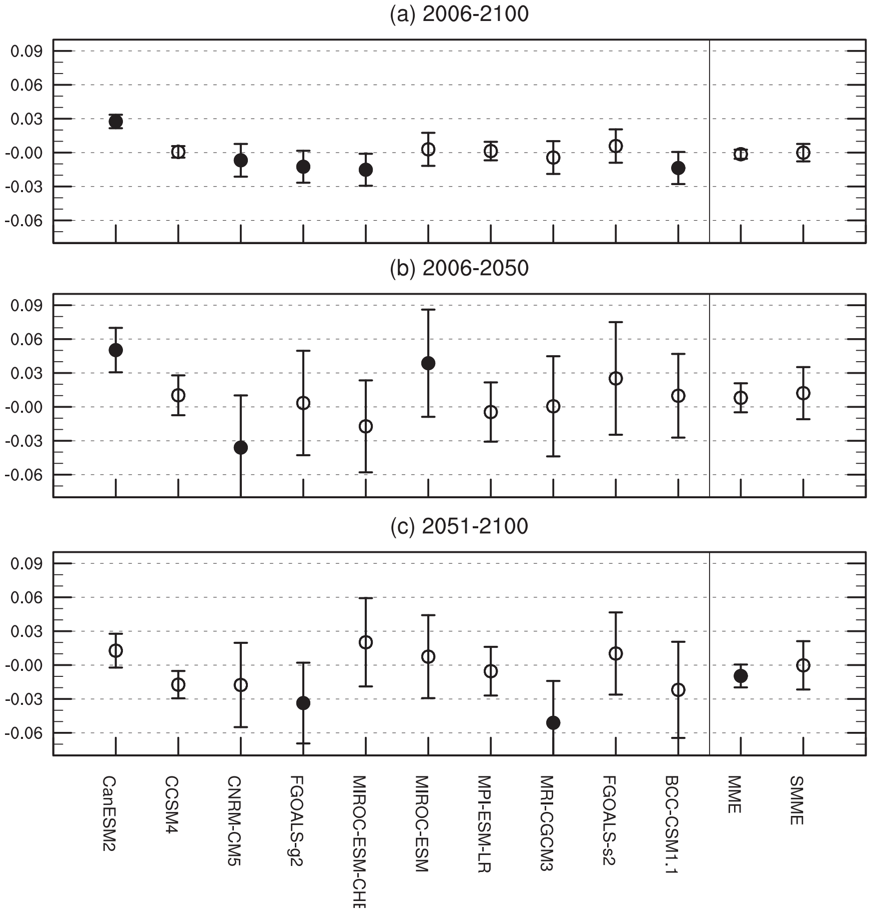

FIG. 10. Linear trend in the SAMI under RCP4.5 during (a) 2006–2100, (b) 2006–50, and (c) 2051–2100. The solid (open) circle indicates significance (no significance) at the 95% confidence level. Error bars as in Fig. 9.

accurately than the longitude, while there is still a considerable amount of latitude spread among the models. In addition, a comparison between Figs. 2 and 3 suggests that most of the models do not capture the latitudinal extent of the cyclonic circulation. The predicted longitude of this cyclonic center varies by more than 90° among the models (i.e., about 1/4 of the longitude circle).

c. *Evaluation of model-simulated SAM temporal variability*

To assess the ability of the CMIP5 models to reproduce the temporal variability of the SAM, we use a selection of methods.

To start with, Fig. 7 shows how the SAMI has evolved since 1950. All 12 models have successfully reproduced the observed positive SAM trend over recent decades; an improvement of CMIP5 compared to CMIP3 and could be attributed to time-variable ozone forcing. However, on interdecadal scales, model performance is generally limited. As mentioned above, decadal negative and positive SAM phases occurred during the periods 1964–70 and 1994–2000, but less than half of these models, including CCSM4, CNRM-CM5, HadCM3, and FGOALS-s2, reproduced these decadal phases. Interannual variability is also visibly larger for the modeled plumes than observed in Figs. 2c and 2d.

We determine quantitatively the correspondence between the modeled and observed (20CR) SAMI using the following three measures: 1) the ratio of standard deviations between modeled and observed SAMI, 2) the statistical significance of the long-term SAMI trend, and 3) the correlation coefficients between modeled and observed detrended SAMI on decadal and interannual time scales.

First, Fig. 8 shows two Taylor diagrams using the same format as in Fig. 4 but for the SAMI. Ratios between the modeled and observed standard deviations (left-hand axis) range from 1.25 to 1.5, confirming the overestimation of modeled SAMI temporal variability noted

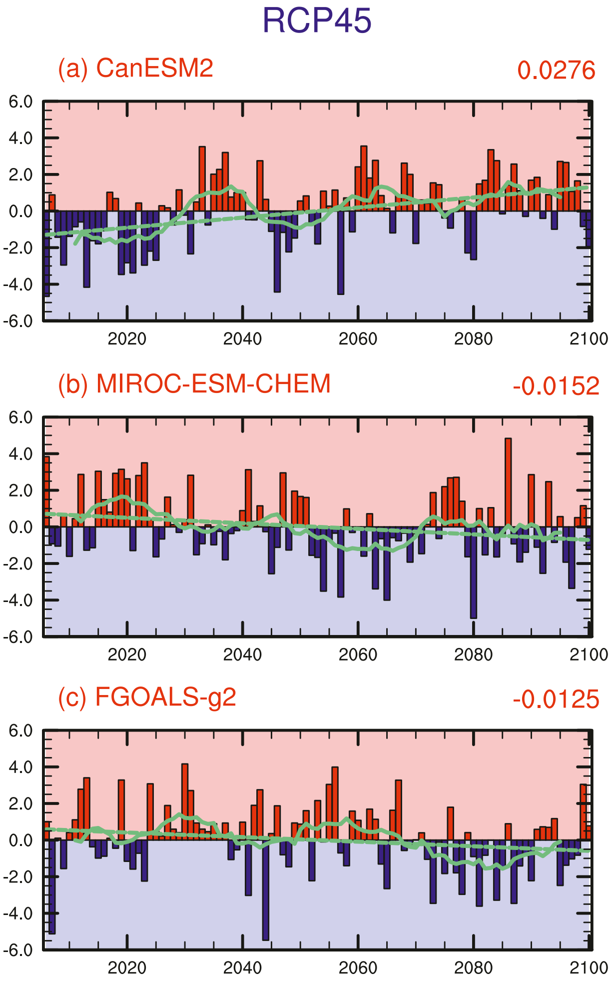

FIG. 11. Projection of the SAMI under RCP4.5 from (a) CanESM2, (b) MIROC-ESM-CHEM, and (c) FGOALS-g2. The straight lines and curves in green represent the linear trend component and decadal variability obtained from the 13-yr weighted running average, respectively. The red numbers are the value of the SAMI slope.

above. The curved axis of Fig. 8 shows the correlations between the modeled and observed time series of the SAMI. The coefficients vary considerably among the models. Some models give statistically significant coefficients (95% confidence level), while others perform less well. HadCM3, for example, has a correlation of 0.5, but MRI-CGCM3 has a value less than 0.1. As in Fig. 4b, the Taylor diagram in Fig. 8b shows results from the first simulation of each model. In comparison with Fig. 8a, it appears that the ensemble size has little influence on the temporal standard deviation ratios, a somewhat surprising result considering the earlier analysis of spatial standard deviation ratios (Fig. 4), which were greatly influenced by the ensemble size.

Second, Fig. 9 shows further statistics regarding the SAMI trend for each model. Most models give a trend (left-hand axis) within the 95% confidence level of the 20CR. The trends of MIROC-ESM-CHEM, BCC_CSM1.1, FGOALS-g2, MIROC-ESM, MPI-ESM-LR, and CanESM2 are the closest to the observations. However, some models, including CNRM-CM5, HadCM3, and CCSM4, show significantly stronger than the observed trend.

Finally, the horizontal axis of Fig. 9 shows the correlation between each model and observations of the detrended SAMI time series. Compared with Fig. 8a, the correlation coefficients generally decrease significantly as a consequence of the detrending. Only three models (HadCM3, FGOALS-g2, and MIROC-ESM-CHEM) give statistically significant correlations (at the 90% level). This suggests that the observed and modeled SAM relationship is partly controlled by the linear trends.

Overall, the three models, FGOALS-g2, MIROC-ESM-CHEM, and CanESM2, performed well in reproducing both observed long-term changes and decadal and interannual variations of the SAM. For this reason, we have selected these three models for the analysis of the future trend in the SAM. However, given that long-term trends are generally handled better than interdecadal variability, we restrict our analysis of future SAM temporal characteristics to the trend.

4. SAM projections for the twenty-first century

Simpkins and Karpechko (2012) assessed future SAM trends using output from the CMIP3 models following selected IPCC AR4 scenarios. We build on their work by using the CMIP5 models and the new IPCC AR5 RCP4.5 and RCP8.5 radiative concentration pathways, whose details were discussed in section 2a.

a. RCP4.5

Figure 10a shows the linear trend in the SAMI for the RCP4.5 path for this century (2006–2100). Both the SMME and equally weighted MME means reveal a weakly negative and statistically insignificant (95% confidence level) trend, yet 5 of the 12 models exhibit a statistically significant (positive or negative) trend. Based on the SMME and MME results, there are no significant long-term changes in the SAMI for the RCP4.5 because of the offset effect of ozone recovery and increasing GHGs, as previous studies (e.g., McLandress et al. 2011) have pointed out.

For a look at changes in the SAM within the twenty-first century, Figs. 10b and 10c show the linear trend in the SAMI for the 2006–50 and 2051–2100 periods,

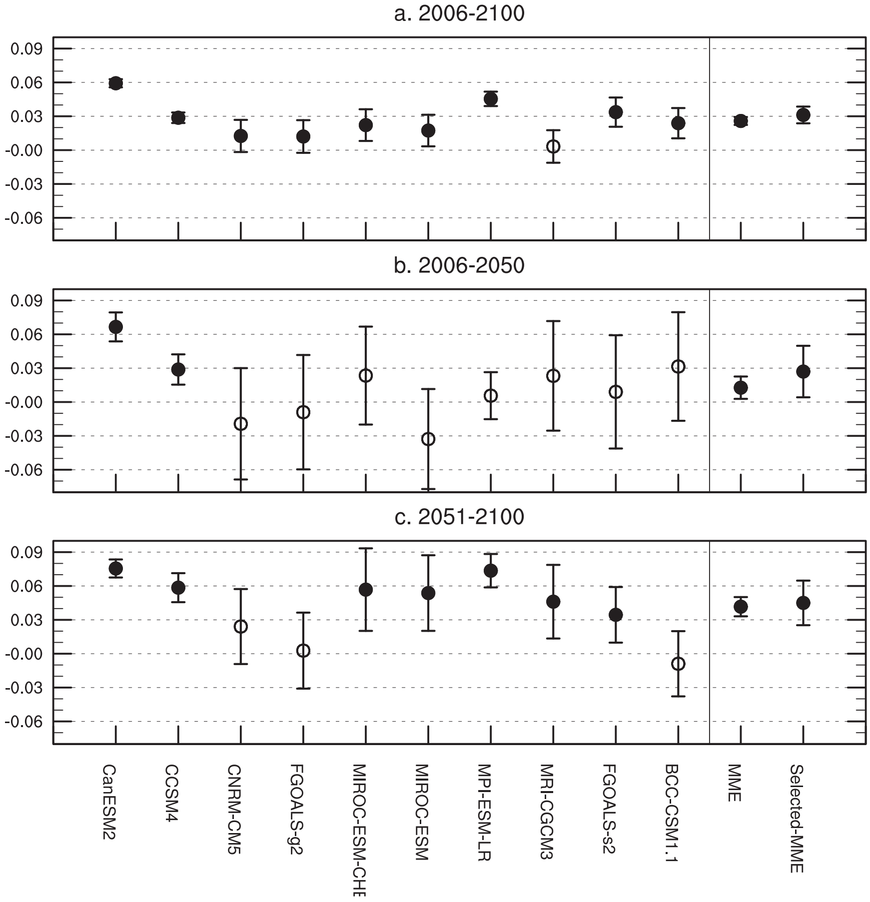

FIG. 12. As in Fig. 10, but for RCP8.5.

respectively. For most models as well as the SMME and MME means, future changes are insignificant. As Fig. 1 shows, because the main external forcing factors (ozone and GHGs) either offset each other or remained almost constant over these two periods, the SAMI under RCP4.5 exhibits an almost negligible trend during both periods.

However, the projections of the SAM in RCP4.5 do show large model uncertainty, indicating how the balance between the ozone and GHGs influences is possibly varying according to models. Although it has been suggested by the MME and SMME means that there is a weak trend in the SAM within the twenty-first century because of the balancing effects of ozone and GHGs forcings, the details of the balance are not entirely understood and are model dependent. Evidence for this is shown in Fig. 11, which shows future SAMI trends for the three models selected for their ability to simulate observed trends. While CanESM2 projects a future significant increase in the SAM, the MIROC-ESM-CHEM and FGOALS-g2 models project decreases.

b. *RCP8.5*

Figure 12 shows results for the RCP8.5 pathway. For the entire century (2006–2100 period), almost all models have significant positive SAMI trends. Compared with RCP4.5, these significant trends imply that the balancing effects of ozone and GHGs forcings are not relevant for this pathway, which is due to the significant increase of GHGs. The SMME and MME means also give magnitudes comparable to the recent trend since 1950. During the first half century, the trend is very close to that in RCP4.5, due to the similarity of the temporal evolution of radiative forcing between RCP4.5 and RCP8.5 (Fig. 1). The difference is that the trends in the RCP4.5 simulations lack statistical significance because the GHGs forcing in RCP4.5 is slightly weaker than that in RCP8.5. Beyond 2050, the trend is considerably larger, possibly due to a lagged accumulative effect of the very rapid increases in radiative forcing in the middle of the century. Moreover, Fig. 13 shows the equivalent trends as in Fig. 11 but for the RCP8.5 pathway. The SAMI in these models all show statistically significant positive

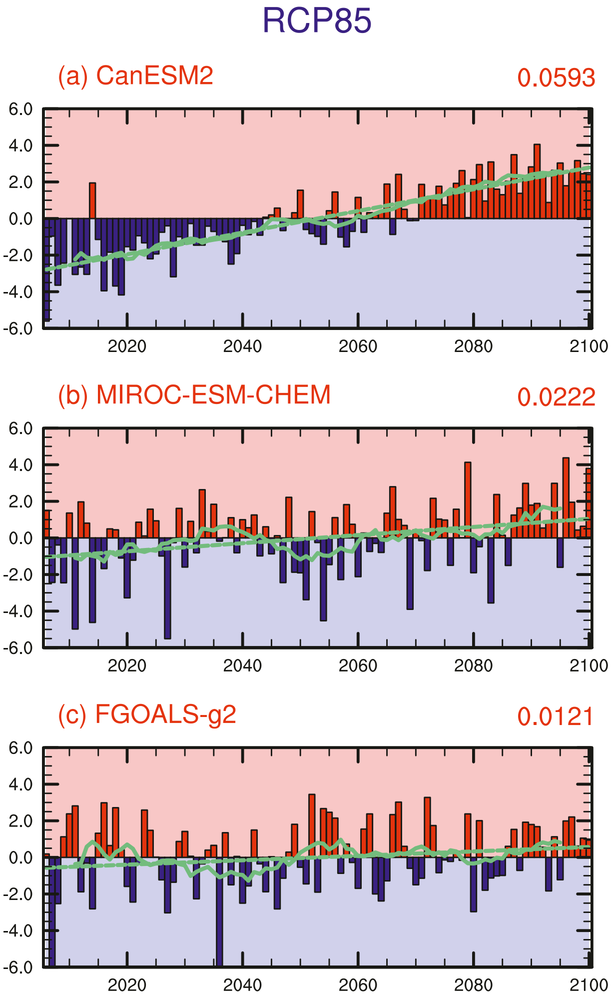

FIG. 13. As in Fig. 11, but for RCP8.5.

trends. This trend is greatest in CanESM2 (0.0593 yr^{-1}) and twice as large as the trend since 1950.

In general, the majority of the 10 models we examine generated consistently positive trends in the SAM under RCP8.5 as a result of the large increases in GHGs. Although ozone forcing falls to zero gradually, the trend in the SAM can also reach the current magnitude as a result of increasing GHGs levels. Beyond 2050, trends in the SAMI are projected to be larger than in the recent past.

5. Analysis of model uncertainty

In the previous section, we noted a discrepancy between the model uncertainties inherent in the sign of future SAM trends between the RCP4.5 and RCP8.5 future pathways. To recap, the RCP4.5 pathway (Fig. 11) gave a significant increasing future trend for CanESM2 but decreasing trends for MIROC-ESM-CHEM and FGOALS-g2, while all three models exhibit increases for the RCP8.5 pathway (Fig. 13). We now examine the possible reasons for this divergent behavior.

From the literature (McLandress et al. 2010; Polvani et al. 2011b; Hegerl et al. 2007), increases in GHGs cool the stratosphere over the polar regions, while increases in stratospheric ozone cause a warming, thus giving opposing influences on the polar stratospheric vortex and in turn the SAM. We hypothesize that these effects contribute to the uncertainty in the sign of future SAM change seen for RCP4.5. Figures 14a–c show the linear trend in the zonal mean temperature for the RCP4.5 pathway. Warming is projected for the troposphere and cooling for the upper stratosphere at most latitudes in the three models. However, poleward of 40°S, at levels in the transition zone (300–50 hPa) between the tropospheric warming and upper-stratospheric cooling, differences in the temperature trend emerge among the models. CanESM2 has weaker warming than MIROC-ESM-CHEM and FGOALS-g2. This suggests a stronger cooling effect caused by GHGs in CanESM2 compared to the other two. The influence is also supported by Figs. 14d–f that show trends in geopotential height for the three models. In the CanESM2 model, the lifting trend in geopotential height over the polar region is smaller. This causes the trend in the gradient of geopotential height to point from the mid- to high latitudes, giving a positive SAMI trend. For the other two models, (and especially FGOALS-g2) the trend direction is reversed with the largest geopotential lifting over the pole, causing the decreasing SAMI trend.

For RCP8.5, an equivalent analysis of temperature and geopotential height changes on the latitude–height profile is presented in Fig. 15. Here, the cooling effect caused by GHGs in the transition zone between the tropospheric warming and upper-stratospheric cooling poleward of 40°S is stronger than that in RCP4.5 in all three models. There is also consistency among the models poleward of 40°S for the simulated geopotential height (Figs. 15e,f). The trends of the gradients point from the mid- to high latitudes in all three models, in accordance with the increasing SAMI trend.

6. Summary and conclusions

This paper investigated the projections of the SAM, which is the principal mode of variability of atmospheric circulation in the SH extratropics, using 12 CMIP5 models based on analysis of their ability to simulate the SAM. Our results have found that the CMIP5 models capture the zonally symmetric as well as the asymmetric components of the SAM reasonably well and typically generate a more realistic simulation of the dipole

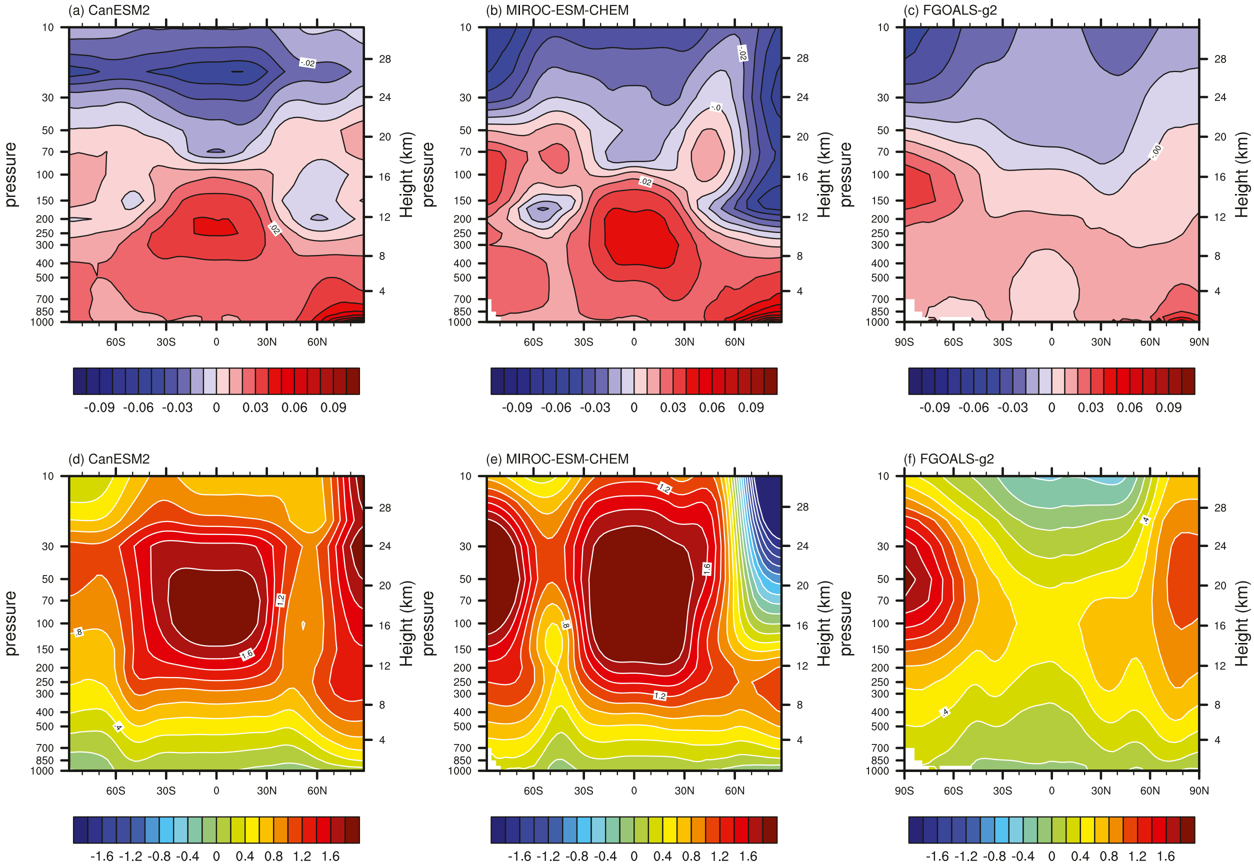
(a) CanESM2 (b) MIROC-ESM-CHEM (c) FGOALS-g2

(d) CanESM2 (e) MIROC-ESM-CHEM (f) FGOALS-g2

FIG. 14. Linear trend in (a)–(c) zonal mean temperature and (d)–(f) geopotential height from (left) CanESM2, (center) MIROC-ESM-CHEM, and (right) FGOALS-g2 under RCP4.5.

structure of the SAM than the CMIP3 models. However, most CMIP5 models appear to overly magnify the proportion of circulation variability associated with the SAM. All 12 models replicate the long-term positive trend in the recently observed SAMI, an improvement compared to CMIP3 due to time-variable ozone forcing. Although the simulation of interdecadal and interannual variability of the SAM by some of models is encouraging, the ability to simulate interannual variability remains generally limited when compared with lower-frequency signals.

Furthermore, models with a higher horizontal resolution, such as CCSM4 and MRI-CGCM3, did not show a superior performance in the SAM pattern simulation. In a recent study, Charlton-Perez et al. (2013) found that both the high-top and low-top (with a threshold at 1 hPa) models can reproduce the past stratospheric temperature trends despite differences in the handling of the stratospheric process in the low-top models. In this work, we further find that there are no significant differences in model performance in capturing the long-term SAMI trend between high-top (e.g., MIROC-ESM-CHEM) and low-top (e.g., FGOALS-g2) models (Fig. 9). This implies that a lack of stratospheric processes higher than 1 hPa may not significantly influence the modeled SAMI on long-term scales. We note, however, that this conclusion is only based on the subset of CMIP5 models and not the entire suite. It is also worth pointing out that the four models (CCSM4, HadCM3, CNRM-CM5, and FGOALS-s2) that best simulate the two observed decadal SAMI phases are all low-top models (Fig. 7). More work needs to be done to explore other CMIP5 models' ability to reproduce the spatial and temporal characteristics of the SAM.

Model projections of the SAM for the twenty-first century up to 2100 were then examined for the IPCC RCP4.5 and RCP8.5 pathways. With the RCP4.5 projections, the opposing influences from GHGs increases and ozone recovery effects on the SAM appear, overall, to largely mitigate each other with the weakly negative SAM trend mostly insignificant during the twenty-first century.

On the other hand, for the RCP8.5 projections significant positive increases in the SAMI are seen for most

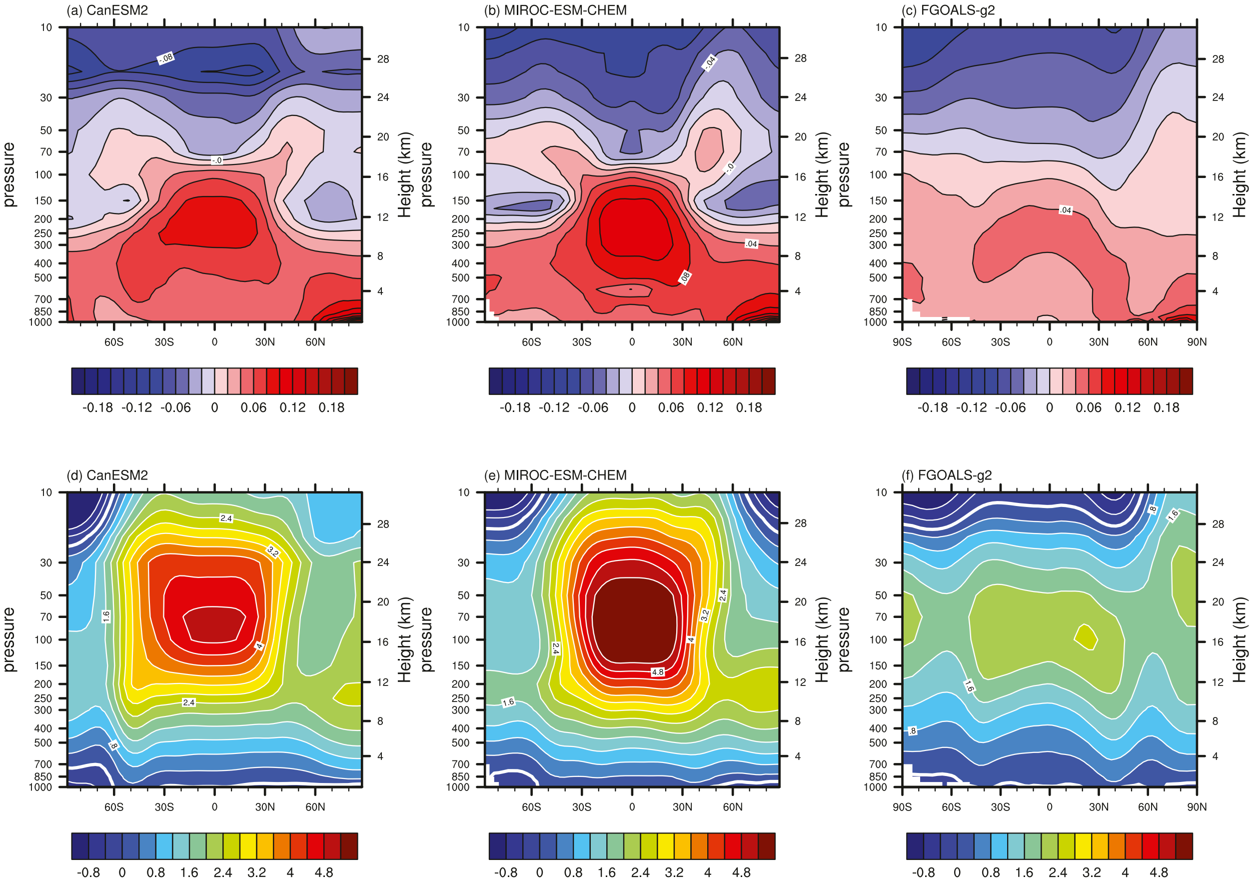

FIG. 15. As in Fig. 14, but for RCP8.5.

models and the ensemble mean for the twenty-first century, indicating that the effects of the GHGs increases outweigh those of the ozone recovery. This is supported by differences between the SAMI trends in the first and second halves of the twenty-first century. Between 2006 and 2050, increases in GHGs and ozone recovery in the CMIP5 models occur together. As a result, a limiting of the positive SAMI trend is seen in some of the projections. Beyond 2050, however, GHGs increases continue, but further ozone recovery is prevented, resulting in stronger positive significant SAMI trends in almost all models. This sensitivity of the SAM to GHGs is in agreement with recent research by Simpkins and Karpechko (2012) using CMIP3 multimodel datasets, although the IPCC AR4 SRES they used were not exactly the same as the IPCC AR5 RCPs used in this work. In addition, consistent with Simpkins and Karpechko (2012), the SAM is projected to experience a very weak trend during the first half of the twenty-first century for both RCP4.5 and RCP8.5 pathways, while in the second half the positive trend depends on the different pathways. The strengthening SAM in the RCP8.5, in turn, may even itself modulate the ozone concentration. Positive phases of the SAM are often linked with decreasing ozone over the following several months (Fogt et al. 2009b). Therefore, the increasing trend in the SAMI caused by GHGs may reduce the ozone concentration and is likely to reduce the impact of decreasing ozone-depleting substances on ozone recovery, which may impede the recovery.

The projections of the SAM under RCP4.5 show large model-related uncertainty. The results show that the simulation of stratospheric temperature in the SH polar region, which is determined by both radiative forcing from ozone and GHGs, is closely related to the simulated SAMI trend. As stratospheric ozone forcing will weaken under RCP4.5 and RCP8.5, the response of stratospheric temperature to GHGs concentrations becomes significant in SAM trend projections. Because of its sensitivity to GHGs, the polar stratospheric temperature can heavily influence the SAM and contribute to the uncertainty in its projection. This suggested an important influence of temperature sensitivity to GHGs in the SH polar region on future SAM evolution.

Acknowledgments. This work was jointly supported by the 973 Program (2010CB950400), the NSFC Key Project (41030961), and the China Special Fund for Meteorological Research in the Public Interest (GYHY201306031). Dr. Robin Clark was supported by the Joint DECC/Defra Met Office Hadley Centre Climate Programme (GA01101). We acknowledge the World Climate Research Programme's Working Group on Coupled Modelling, which is responsible for CMIP, and we thank the climate modeling groups (listed in Table 1 of this paper) for producing and making available their model output. Support of this dataset is provided by the Office of Science, U.S. Department of Energy in partnership with the Global Organization for Earth System Science Portals. Thanks to the editor Dr. John Chiang and the two anonymous reviewers; their comments and suggestions helped us to improve the manuscript.

REFERENCES

Arblaster, J. M., and G. A. Meehl, 2006: Contributions of external forcings to southern annular mode trends. *J. Climate,* **19,** 2896–2905.

Bao, Q., and Coauthors, 2013: The Flexible Global Ocean-Atmosphere-Land System Model, version 2: FGOALS-s2. *Adv. Atmos. Sci.,* **30,** 561–576.

Bromwich, D. H., and R. L. Fogt, 2004: Strong trends in the skill of the ERA-40 and NCEP–NCAR reanalyses in the high and midlatitudes of the Southern Hemisphere, 1958–2001. *J. Climate,* **17,** 4603–4619.

Cai, W. J., and T. Cowan, 2007: Trends in Southern Hemisphere circulation in IPCC AR4 models over 1950–99: Ozone depletion versus greenhouse forcing. *J. Climate,* **20,** 681–693.

Charlton-Perez, A. J., and Coauthors, 2013: On the lack of stratospheric dynamical variability in low-top versions of the CMIP5 models. *J. Geophys. Res.,* **118,** 2494–2505, doi:10.1002/jgrd.50125.

Chylek, P., J. Li, M. K. Dubey, M. Wang, and G. Lesins, 2011: Observed and model simulated 20th century Arctic temperature variability: Canadian Earth System Model CanESM2. *Atmos. Chem. Phys. Discuss.,* **11,** 22 893–22 907.

Ciasto, L. M., and D. W. J. Thompson, 2008: Observations of large-scale ocean–atmosphere interaction in the Southern Hemisphere. *J. Climate,* **21,** 1244–1259.

——, M. A. Alexander, C. Deser, and M. H. England, 2011: On the persistence of cold-season SST anomalies associated with the annular modes. *J. Climate,* **24,** 2500–2515.

Compo, G. P., and Coauthors, 2011: The Twentieth Century Reanalysis Project. *Quart. J. Roy. Meteor. Soc.,* **137,** 1–28.

Deser, C., A. Phillips, V. Bourdette, and H. Y. Teng, 2012: Uncertainty in climate change projections: The role of internal variability. *Climate Dyn.,* **38,** 527–546.

Fan, K., 2007: Zonal asymmetry of the Antarctic Oscillation. *Geophys. Res. Lett.,* **34,** L02706, doi:10.1029/2006GL028045.

Feng, J., J. P. Li, and Y. Li, 2010: Is there a relationship between the SAM and southwest Western Australian winter rainfall? *J. Climate,* **23,** 6082–6089.

——, ——, and H. L. Xu, 2013: Increased summer rainfall in northwest Australia linked to southern Indian Ocean climate variability. *J. Geophys. Res.,* **118,** 467–480, doi:10.1029/2012JD018323.

Fogt, R. L., J. Perlwitz, A. J. Monaghan, D. H. Bromwich, J. M. Jones, and G. J. Marshall, 2009a: Historical SAM variability. Part II: Twentieth-century variability and trends from reconstructions, observations, and the IPCC AR4 models. *J. Climate,* **22,** 5346–5365.

——, ——, S. Pawson, and M. A. Olsen, 2009b: Intra-annual relationships between polar ozone and the SAM. *Geophys. Res. Lett.,* **36,** L04707, doi:10.1029/2008GL036627.

Gent, P. R., and Coauthors, 2011: The Community Climate System Model version 4. *J. Climate,* **24,** 4973–4991.

Gillett, N. P., and D. W. J. Thompson, 2003: Simulation of recent Southern Hemisphere climate change. *Science,* **302,** 273–275.

Gong, D. Y., and S. W. Wang, 1998: Antarctic Oscillation: Concept and applications. *Chin. Sci. Bull.,* **43,** 734–738.

——, and ——, 1999: Definition of Antarctic Oscillation index. *Geophys. Res. Lett.,* **26,** 459–462.

——, and ——, 2001: Decadal variability of the Antarctic Oscillation. *Acta Meteor. Sin.,* **15,** 178–190.

——, S. J. Kim, and C. H. Ho, 2009: Arctic and Antarctic Oscillation signatures in tropical coral proxies over the South China Sea. *Ann. Geophys.,* **27,** 1979–1988.

Gordon, C., C. Cooper, C. A. Senior, H. Banks, J. M. Gregory, T. C. Johns, J. F. B. Mitchell, and R. A. Wood, 2000: The simulation of SST, sea ice extents and ocean heat transports in a version of the Hadley Centre coupled model without flux adjustments. *Climate Dyn.,* **16,** 147–168.

Grassi, B., G. Redaelli, and G. Visconti, 2005: Simulation of polar Antarctic trends: Influence of tropical SST. *Geophys. Res. Lett.,* **32,** L23806, doi:10.1029/2005GL023804.

Hegerl, G. C., and Coauthors, 2007: Understanding and attributing climate change. *Climate Change 2007: The Physical Science Basis,* S. Solomon et al., Eds., Cambridge University Press, 663–745.

Hendon, H. H., D. W. J. Thompson, and M. C. Wheeler, 2007: Australian rainfall and surface temperature variations associated with the Southern Hemisphere annular mode. *J. Climate,* **20,** 2452–2467.

Jiang, Y., Y. Luo, and Z. C. Zhao, 2010: Projection of wind speed changes in China in the 21st century by climate models. *Chin. J. Atmos. Sci.,* **34,** 323–336.

Kalnay, E., and Coauthors, 1996: The NCEP/NCAR 40-Year Reanalysis Project. *Bull. Amer. Meteor. Soc.,* **77,** 437–471.

Kang, S. M., L. M. Polvani, J. C. Fyfe, and M. Sigmond, 2011: Impact of polar ozone depletion on subtropical precipitation. *Science,* **332,** 951–954.

Kwok, R., and J. C. Comiso, 2002: Southern Ocean climate and sea ice anomalies associated with the Southern Oscillation. *J. Climate,* **15,** 487–501.

Lefebvre, W., H. Goosse, R. Timmermann, and T. Fichefet, 2004: Influence of the southern annular mode on the sea ice–ocean system. *J. Geophys. Res.,* **109,** C09005, doi:10.1029/2004jc002403.

Li, J. P., and J. X. L. Wang, 2003: A modified zonal index and its physical sense. *Geophys. Res. Lett.,* **30,** 1632, doi:10.1029/2003GL017441.

——, and Coauthors, 2011a: *Ocean-Atmosphere Interaction over the Joining Area of Asia and Indian-Pacific Ocean and Its Impact on the Short-Term Climate Variation in China* (in Chinese). Vol. I. China Meteorological Press, 516 pp.

——, and Coauthors, 2011b: *Ocean-Atmosphere Interaction over the Joining Area of Asia and Indian-Pacific Ocean and Its*

Impact on the Short-Term Climate Variation in China (in Chinese). Vol. II. China Meteorological Press, 565 pp.

——, and Coauthors, 2013: Progress in air–land–sea interactions in Asia and their role in global and Asian climate change (in Chinese). *Chin. J. Atmos. Sci.,* **37,** 518–538.

Li, X. F., and J. P. Li, 2009: Main submonthly timescales of Northern and Southern Hemispheres annual modes (in Chinese). *Chin. J. Atmos. Sci.,* **33,** 215–231.

——, and ——, 2010: Propagation characteristics of atmospheric circulation anomalies of sub-monthly Southern Hemisphere annular mode (in Chinese). *Chin. J. Atmos. Sci.,* **34,** 1099–1113.

——, and ——, 2011: Meridional and vertical propagation characteristics of the submonthly Northern Hemisphere annular mode (in Chinese). *Acta Meteor. Sin.,* **69,** 1046–1061.

——, and ——, 2012: Analysis of the quasi-geostrophic adjustment process of the Southern Hemisphere annular mode (in Chinese). *Chin. J. Atmos. Sci.,* **36,** 755–768.

Limpasuvan, V., and D. L. Hartmann, 1999: Eddies and the annular modes of climate variability. *Geophys. Res. Lett.,* **26,** 3133–3136.

Liu, S., and H. J. Wang, 2013: Transition of zonal asymmetry of the Arctic Oscillation and the Antarctic Oscillation at the end of 1970s. *Adv. Atmos. Sci.,* **30,** 41–47.

Lorenz, D. J., and D. L. Hartmann, 2001: Eddy-zonal flow feedback in the Southern Hemisphere. *J. Atmos. Sci.,* **58,** 3312–3327.

Marshall, G. J., 2003: Trends in the southern annular mode from observations and reanalyses. *J. Climate,* **16,** 4134–4143.

——, P. A. Stott, J. Turner, W. M. Connolley, J. C. King, and T. A. Lachlan-Cope, 2004: Causes of exceptional atmospheric circulation changes in the Southern Hemisphere. *Geophys. Res. Lett.,* **31,** L14205, doi:10.1029/2004GL019952.

——, A. Orr, N. P. M. van Lipzig, and J. C. King, 2006: The impact of a changing Southern Hemisphere annular mode on Antarctic Peninsula summer temperatures. *J. Climate,* **19,** 5388–5404.

——, S. Di Battista, S. S. Naik, and M. Thamban, 2011: Analysis of a regional change in the sign of the SAM-temperature relationship in Antarctica. *Climate Dyn.,* **36,** 277–287.

McLandress, C., A. I. Jonsson, D. A. Plummer, M. C. Reader, J. F. Scinocca, and T. G. Shepherd, 2010: Separating the dynamical effects of climate change and ozone depletion. Part I: Southern Hemisphere stratosphere. *J. Climate,* **23,** 5002–5020.

——, T. G. Shepherd, J. F. Scinocca, D. A. Plummer, M. Sigmond, A. I. Jonsson, and M. C. Reader, 2011: Separating the dynamical effects of climate change and ozone depletion. Part II: Southern Hemisphere troposphere. *J. Climate,* **24,** 1850–1868.

Meinshausen, M., and Coauthors, 2011: The RCP greenhouse gas concentrations and their extensions from 1765 to 2300. *Climatic Change,* **109,** 213–241.

Meneghini, B., I. Simmonds, and I. N. Smith, 2007: Association between Australian rainfall and the southern annular mode. *Int. J. Climatol.,* **27,** 109–121.

Nan, S. L., and J. P. Li, 2003: The relationship between the summer precipitation in the Yangtze River valley and the boreal spring Southern Hemisphere annular mode. *Geophys. Res. Lett.,* **30,** 2266, doi:10.1029/2003GL018381.

——, and ——, 2005a: The relationship between the summer precipitation in the Yangtze River valley and the boreal spring Southern Hemisphere annular mode: I. Basic facts (in Chinese). *Acta Meteor. Sin.,* **63,** 837–846.

——, and ——, 2005b: The relationship between the summer precipitation in the Yangtze River valley and the boreal spring Southern Hemisphere annular mode: II. The role of the Indian Ocean and South China Sea as an "oceanic bridge" (in Chinese). *Acta Meteor. Sin.,* **63,** 847–856.

——, ——, X. J. Yuan, and P. Zhao, 2009: Boreal spring Southern Hemisphere annular mode, Indian Ocean sea surface temperature, and East Asian summer monsoon. *J. Geophys. Res.,* **114,** D02103, doi:10.1029/2008JD010045.

Polvani, L. M., M. Previdi, and C. Deser, 2011a: Large cancellation, due to ozone recovery, of future Southern Hemisphere atmospheric circulation trends. *Geophys. Res. Lett.,* **38,** L04707, doi:10.1029/2011GL046712.

——, D. W. Waugh, G. J. P. Correa, and S. W. Son, 2011b: Stratospheric ozone depletion: The main driver of twentieth-century atmospheric circulation changes in the Southern Hemisphere. *J. Climate,* **24,** 795–812.

Previdi, M., and B. G. Liepert, 2007: Annular modes and Hadley cell expansion under global warming. *Geophys. Res. Lett.,* **34,** L22701, doi:10.1029/2007GL031243.

Renwick, J., and D. W. J. Thompson, 2006: The southern annular mode and New Zealand climate. *Water Atmos.,* **14,** 24–25.

Schneider, D. P., E. J. Steig, and J. C. Comiso, 2004: Recent climate variability in Antarctica from satellite-derived temperature data. *J. Climate,* **17,** 1569–1583.

Screen, J. A., N. P. Gillett, A. Y. Karpechko, and D. P. Stevens, 2010: Mixed layer temperature response to the southern annular mode: Mechanisms and model representation. *J. Climate,* **23,** 664–678.

Sen Gupta, A., and M. H. England, 2006: Coupled ocean–atmosphere–ice response to variations in the southern annular mode. *J. Climate,* **19,** 4457–4486.

Shindell, D. T., and G. A. Schmidt, 2004: Southern Hemisphere climate response to ozone changes and greenhouse gas increases. *Geophys. Res. Lett.,* **31,** L18209, doi:10.1029/2004GL020724.

Simpkins, G. R., and A. Y. Karpechko, 2012: Sensitivity of the southern annular mode to greenhouse gas emission scenarios. *Climate Dyn.,* **38,** 563–572.

——, L. M. Ciasto, D. W. J. Thompson, and M. H. England, 2012: Seasonal relationships between large-scale climate variability and Antarctic sea ice concentration. *J. Climate,* **25,** 5451–5469.

Song, J., W. Zhou, C. Y. Li, and L. X. Qi, 2009: Signature of the Antarctic Oscillation in the Northern Hemisphere. *Meteor. Atmos. Phys.,* **105,** 55–67.

Storch, H. V., and F. W. Zwiers, 1999: Eigen techniques. *Statistical Analysis in Climate Research,* Cambridge University Press, 293–312.

Sun, C., and J. P. Li, 2012: Space–time spectral analysis of the Southern Hemisphere daily 500-hPa geopotential height. *Mon. Wea. Rev.,* **140,** 3844–3856.

Taylor, K. E., 2001: Summarizing multiple aspects of model performance in a single diagram. *J. Geophys. Res.,* **106** (D7), 7183–7192.

——, R. J. Stouffer, and G. A. Meehl, 2012: An overview of CMIP5 and the experiment design. *Bull. Amer. Meteor. Soc.,* **93,** 485–498.

Thompson, D. W. J., and J. M. Wallace, 2000: Annular modes in the extratropical circulation. Part I: Month-to-month variability. *J. Climate,* **13,** 1000–1016.

——, and S. Solomon, 2002: Interpretation of recent Southern Hemisphere climate change. *Science,* **296,** 895–899.

——, J. M. Wallace, and G. C. Hegerl, 2000: Annular modes in the extratropical circulation. Part II: Trends. *J. Climate,* **13,** 1018–1036.

——, S. Solomon, P. J. Kushner, M. H. England, K. M. Grise, and D. J. Karoly, 2011: Signatures of the Antarctic ozone hole in Southern Hemisphere surface climate change. *Nat. Geosci.,* **4,** 741–749.

Visbeck, M., 2009: A station-based southern annular mode index from 1884 to 2005. *J. Climate,* **22,** 940–950.

Voldoire, A., and Coauthors, 2013: The CNRM-CM5.1 global climate model: Description and basic evaluation. *Climate Dyn.,* **40,** 2091–2121, doi:10.1007/s00382-011-1259-y.

Watanabe, S., and Coauthors, 2011: MIROC-ESM 2010: Model description and basic results of CMIP5-20c3m experiments. *Geosci. Model Dev.,* **4,** 845–872.

Wilks, R. A., 2006: Principal component (EOF) analysis. *Statistical Methods in the Atmospheric Sciences,* Elsevier, 463–507.

Wu, Z. W., J. P. Li, J. H. He, and Z. H. Jiang, 2006a: Occurrence of droughts and floods during the normal summer monsoons in the mid- and lower reaches of the Yangtze River. *Geophys. Res. Lett.,* **33,** L05813, doi:10.1029/2005GL024487.

——, ——, ——, and ——, 2006b: Large-scale atmospheric singularities and summer long-cycle droughts-floods abrupt alternation in the middle and lower reaches of the Yangtze River. *Chin. Sci. Bull.,* **51,** 2027–2034.

——, ——, B. Wang, and X. H. Liu, 2009: Can the Southern Hemisphere annular mode affect China winter monsoon? *J. Geophys. Res.,* **114,** D11107, doi:10.1029/2008JD011501.

Yu, Y. Q., W. P. Zheng, B. Wang, H. L. Liu, and J. P. Liu, 2011: Versions g1.0 and g1.1 of the LASG/IAP Flexible Global Ocean-Atmosphere-Land System Model. *Adv. Atmos. Sci.,* **28,** 99–117.

Yuan, X. J., and E. Yonekura, 2011: Decadal variability in the Southern Hemisphere. *J. Geophys. Res.,* **116,** D19115, doi:10.1029/2011JD015673.

Yukimoto, S., and Coauthors, 2012: A new global climate model of the Meteorological Research Institute: MRI-CGCM3—Model description and basic performance. *J. Meteor. Soc. Japan,* **90A,** 23–64.

Zheng, F., and J. P. Li, 2012: Impact of preceding boreal winter Southern Hemisphere annular mode on spring precipitation over south China and related mechanism (in Chinese). *Chin. J. Geophys.,* **55,** 3542–3557.

Zhu, Y. L., and H. J. Wang, 2008: The Arctic and Antarctic Oscillations in the IPCC AR4 coupled models (in Chinese). *Acta Meteor. Sin.,* **66,** 993–1004.